[Geophysical Research Letters]

Supporting Information for

[Aeromagnetic, gravity, and Differential Interferometric Synthetic Aperture Radar (DInSAR) analyses reveal the causative fault of the April 3, 2017 *M*w 6.5 Moiyabana, Botswana Earthquake]

[F. Kolawole[1], E. A. Atekwana[1], S. Malloy[2], D. S. Stamps[2], R. Grandin[3], M. G. Abdelsalam[1], K. Leseane[4] and E. M. Shemang[5]]

[[1]Oklahoma State University Main Campus, Stillwater, OK, United States; [2]Department of Geosciences, Virginia Tech, Blacksburg, VA, United States; [3]Université Paris Diderot, Paris, France; [4]School of Earth Atmosphere and Environment, Monash University, Melbourne, Australia; [5]Botswana International University of Science and Technology, Palapye, Botswana]

Contents of this file

Introduction

The supporting information below include a description of some of the processing techniques applied to the gravity and aeromagnetic data covering the study area- the Moiyabana area of eastern Botswana. The material also contains two examples that illustrate our approach for assessing the preferred fault geometry model. The gravity and aeromagnetic data used in this study were obtained from the Geological Survey of Botswana (now Botswana Geoscience Institute). The obtained aeromagnetic data is a grid of the IGRF corrected total magnetic

intensity (TMI) data. In this study, all aeromagnetic, gravity and DInSAR data are referenced to the World Geodetic System 1984 (WGS84) datum.

Text S1. Detailed information on the gravity anomaly data and aeromagnetic data used in this study are provided in Tables S1 and S2. The land gravity data used in this study includes three datasets. The first dataset consists of the land gravity data acquired in 1972-1973 at 10 km station spacing [*Reeves and Hutchins*, 1976]. The second dataset consists of an infill land gravity survey that was carried out in 1998-1999 at 7.5 km station spacing in the northern part of Botswana. The third dataset consists of land gravity data provided by the mining industry and academic institution, acquired at variable station spacing. The observed gravity readings were corrected for instrumental drift, tidal effects, latitude, and heights, with emphasis on standard field procedures for monitoring accuracy of the observed gravity reading. The GPS and observed measurements were reduced to the WGS84 datum. The Bouguer gravity anomalies were calculated using the 1967 International gravity formula using the mean crustal rock density of 2.67 g/cc. The compiled gravity data was regridded with a 1 km cell size using a minimum curvature technique [*Swain, 1976; Briggs, 1974*] (Figures S2a-b). The TMI aeromagnetic data used in this study was also gridded using a minimum curvature technique with 50 m cell size (Figures S2c-d). Both the gravity and aeromagnetic data were provided as Geosoft grids by the Botswana Geoscience Institute.

After gridding, the aeromagnetic field data was reduced to pole (RTP) [*Baranov*, 1957; *Arkani-Hamed*, 1988] in order to remove the skewness of the anomalies and directly position aeromagnetic anomalies over their sources. RTP makes it possible for us to correlate the anomalies with geological information. To enhance edges and field gradients associated with Precambrian basement structures, we applied mathematical filters to the gridded gravity and

52 TMI aeromagnetic maps. The filters include the vertical derivative, horizontal derivative in the *x*
53 and *y* directions and tilt-angle derivative [*Miller and Singh*, 1994; *Blakely*, 1995; *Salem et al.*,
54 2008].

55 To enhance aeromagnetic anomalies within the epicentral area associated with deep
56 structures (characterized by long wavelength and low frequency lineaments) and suppress
57 anomalies associated with shallow sources (characterized by short wavelength and high
58 frequency signals), we applied the low-pass (6 km) and upward-continuation (1 km) filters to
59 the gridded data. The upward continuation filter [*Henderson and Zietz*, 1949; *Jacobsen*, 1987]
60 typically attenuates high wave number anomalies related to shallow magnetic sources, thereby
61 isolating deep magnetic sources. The filter allows quantitative overburden stripping through a
62 simple shift of the datum plane, which allows us to assess the vertical changes in the three-
63 dimensional geometry of a magnetic source. Processing and filtering of both the gravity and
64 aeromagnetic data were implemented in Geosoft's Oasis montaj software.

65 Within the epicentral area, we delineate the possible subsurface geometries of target
66 low frequency magnetic lineaments by evaluating the lateral and vertical variation in magnetic
67 susceptibilities of crustal materials using the three-dimensional (3D) inversion of the IGRF-
68 corrected aeromagnetic data. MAG3D was developed by the University of British Columbia,
69 based on the algorithm of *Li and Oldenburg* [1996]. Following the methodology described in
70 *Leseane et al.* [2015], we windowed a 1° x 1° grid covering the *M*w 6.5 epicentral area (within
71 the boxed area in Figures 1b and S2a-d). Using the MAG3D inversion software, we generated
72 3D block models using a 900 x 900 m mesh cell size and an allowance of 2 km outside the block
73 in order to minimize boundary effect within the target area during the inversion process. The
74 inversion converged after 34 iterations, to a target misfit equal to the number of data points.

After running 3D inversion of the aeromagnetic data using the prepared block model, we obtained a cross-section along a NE-SW transect that cuts across the earthquake epicentral area. In Figure S3, we present the observed, predicted and 'observed minus predicted' magnetic anomalies, along with absolute errors from a 1° × 1° sub-region (shown in Figure 4a) from our 3-D inversion.

To assess our fault geometry models we first balanced predicted and observed seismic moment. We then calculated RMS values for predicted vertical displacements with vertical offsets from InSAR observations described in Section 2.1 using the following equation:

$$RMS = n^{-1} \sum \sqrt{(v_{InSAR} - v_{model})^2}$$

where *n* is the number of surface grid points and *v* is vertical displacement. Our preferred model matches the seismic moment with an RMS of 3.3 cm. For each of the 25 models developed in this study, we solve for static surface displacements with the amount of imposed slip and area of slip on distribution constrained by the total seismic moment calculation. In this approach we assume surface displacements are due to a simple elastic response to stress changes, therefore any additional processes that could influence surface displacements, such as gravitational potential energy gradients due to lateral variations in the Kalahari sediment thicknesses (see Figure 1) or post-seismic effects that could be captured in the InSAR, are unaccounted. In Figure S4, we provide 3 examples of the residual calculations for models. Our preferred model is represented as Figure S4b.

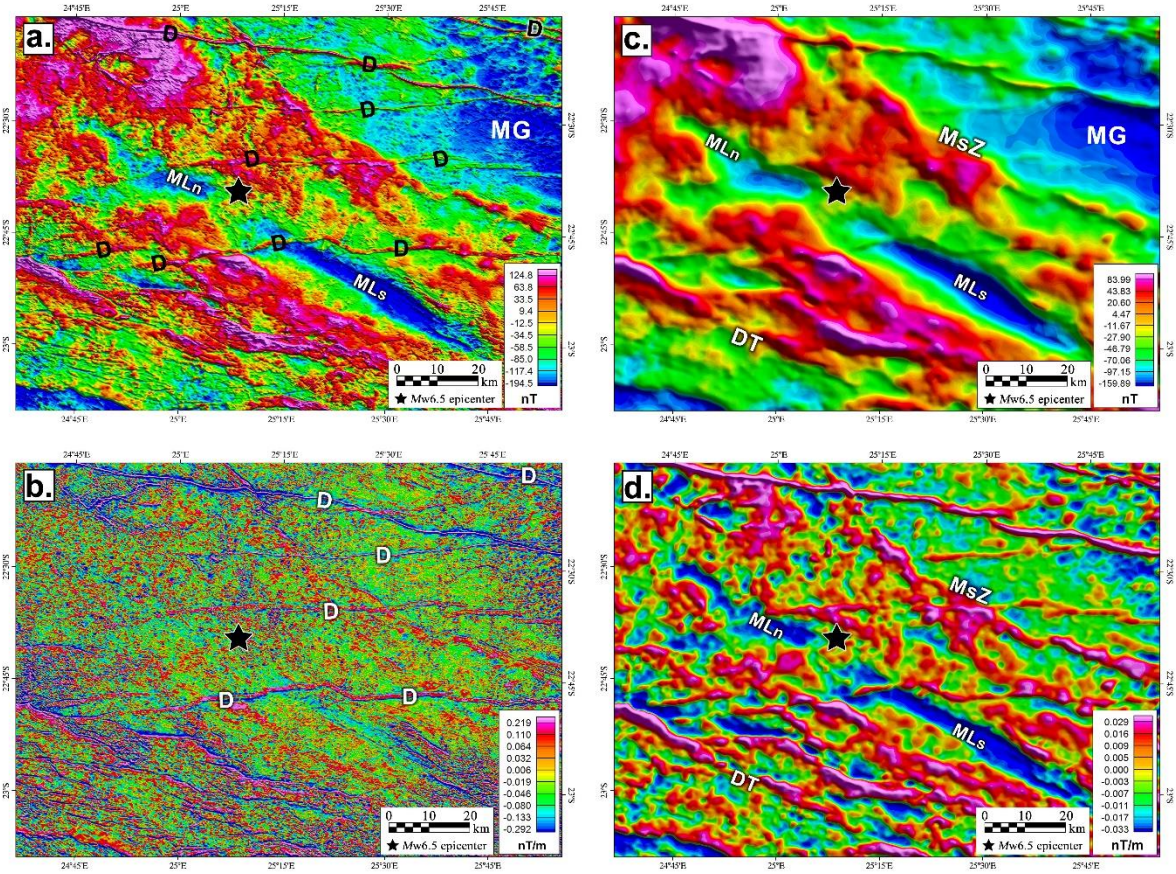

Figure S1. (a) Total magnetic field intensity map of the epicentral region of the 2017 Moiyabana earthquake. (b) Vertical derivative (VDR) of aeromagnetic map in Figure S1a. Notice the dominance of high frequency anomalies (dikes). (c) 1 km upward continuation of the aeromagnetic map in Figure S1a in which high frequency anomalies are suppressed and low frequency anomalies dominate. (d) VDR of 1 km upward-continued aeromagnetic map in Figure S1c, showing enhanced low frequency anomalies and some of the high frequency anomalies. D = Dikes, DT = Dinokwe Thrust, MG = Mahalapye Granite, MLn = northern segment of Moiyabana Lineament (ML), MLs = southern segment of Moiyabana Lineament (ML), MsZ = Mahalapye Shear Zone. Black star represents the epicenter of the *M*w 6.5 Moiyabana earthquake.

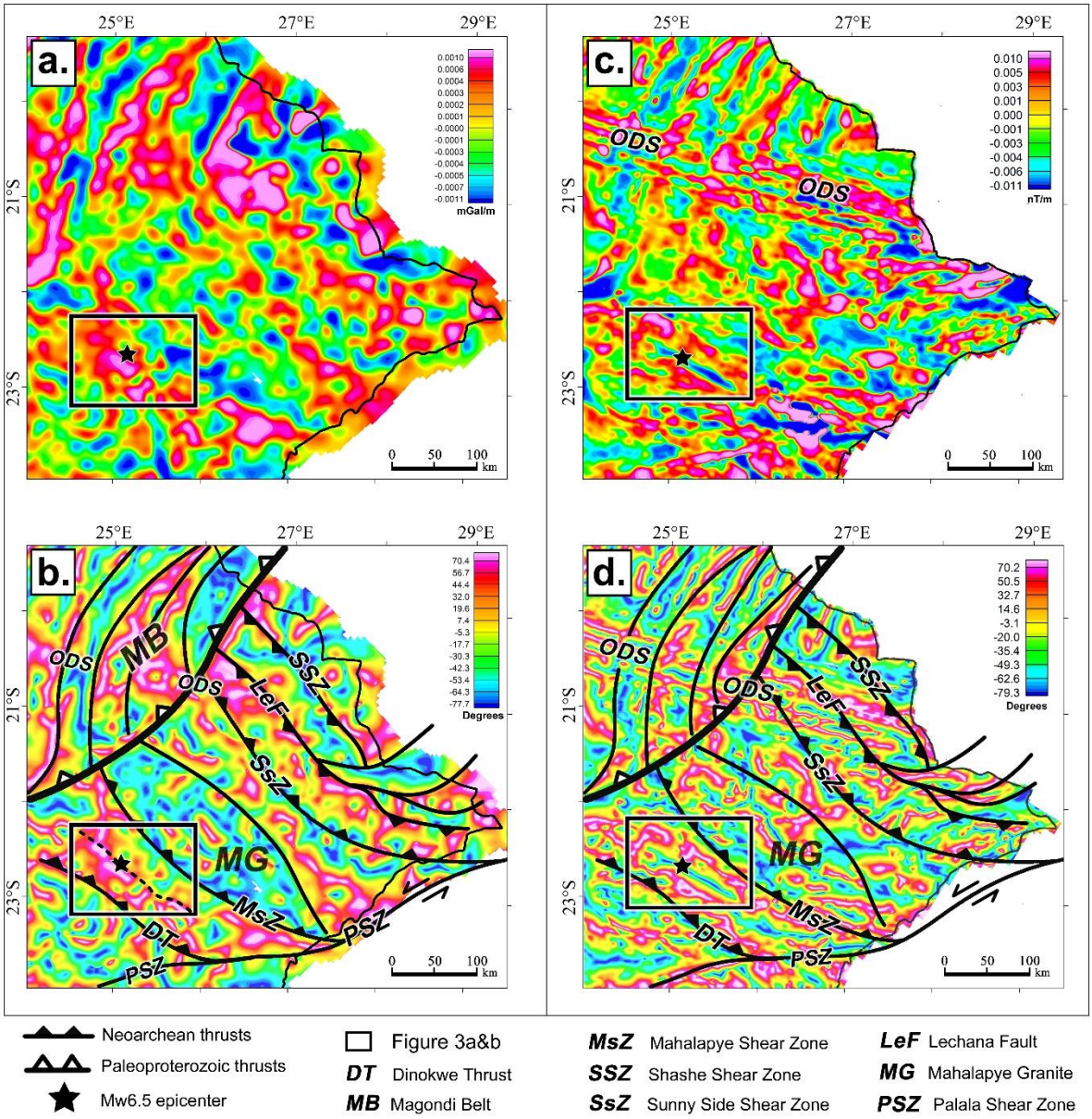

112

Figure S2. (a) Vertical derivative of 1 km upward continued Bouguer anomaly map of eastern Botswana. (b) Tilt-angle derivative of the 1 km upward continued Bouguer anomaly map of eastern Botswana, overlaid with tectonic interpretation from Ranganai et al. [2002]. (c) Vertical derivative of 5 km upward continued aeromagnetic map of eastern Botswana. (d) Tilt-angle derivative of the 5 km upward continued aeromagnetic map of eastern Botswana, overlaid with tectonic interpretation. Open black rectangle represents areas shown in Figures 2, 3, 4 and S1. Black star represents epicenter of the *M*w 6.5 Moiyabana earthquake. ODS = Okavango Dike Swarm.

113

114

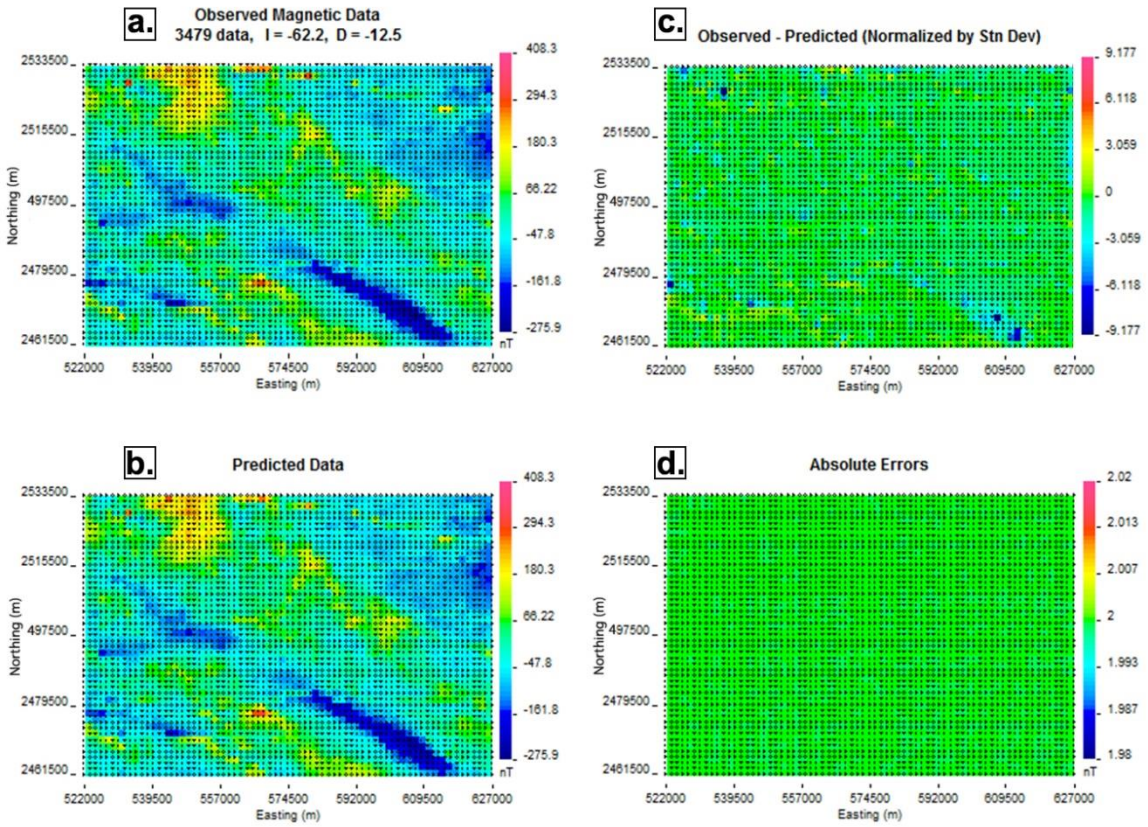

Figure S3. (a) Observed, (b) Predicted, (c) 'Observed minus predicted' magnetic anomalies of the three dimensional magnetic inversion model of the 1° × 1° block shown in Figure 4a. (d) Absolute Errors of the inversion.

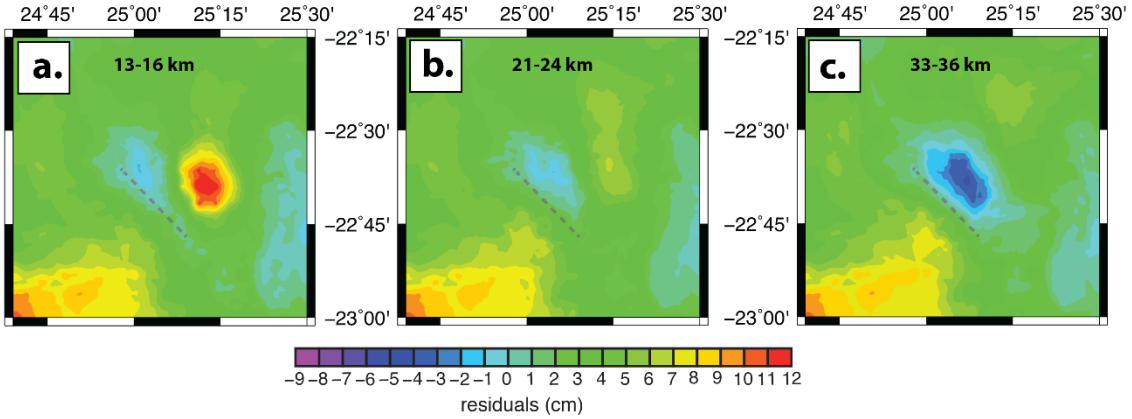

Figure S4. Residual calculations of InSAR vertical offsets and modeled vertical displacements assuming slip occurs on a fault geometry consistent with the USGS focal plane solution. (a) Slip occurs between 13-16 km. (b) Slip occurs between 21-24 km. (c) Slip occurs between 33-36 km.

Gravity Data Documentation					
Data Type	**Data Source**	**Data Spacing**	**Datum**	**Data Reduction**	**Data format**
Land gravity data	Botswana Geoscience Institute	Variable	World Geodetic System 1984 (WGS84)	1967 International Gravity formula	grid

Gridding Method	**Cell Size**	**Grid Filtering**
Minimum curvature	1 km	- 1 km upward continuation - Vertical derivative - Tilt derivative

126 **Table S1.** Table shows detailed information on gravity data documentation and filtering.

127

128

129

Aeromagnetic Data Documentation					
Data Type	**Datum**	**Data Source**	**Acquisition Date**	**Flight Height**	**Line Spacing / Tie-line**
Airbone magnetic data (IGRF-corrected Total Magnetic Intensity)	World Geodetic System 1984 (WGS84)	Botswana Geoscience Institute	1996	80 m	250 m N-S / 1.25 km E-W

			Data Processing		
Data format	**Gridding Method**	**Cell Size**	**Magnetization**	**Reduction to Magnetic Pole**	**Grid Filtering**
grid	Minimum curvature	50 m	Assumed induced magnetization *(no information on remanent magnetization)*	Yes	- Vertical derivative - Tilt-angle derivative - 1 km & 5 km upward continuation - 6 km low-pass

130

131 **Table S2.** Table shows detailed information on aeromagnetic data documentation and
132 processing techniques.